Correlative Optical and X-Ray Imaging of Strain Evolution During Double-Torsion Fracture Toughness Measurements in Shale

Michael R. Chandler[1] [ID], **Anne-Laure Fauchille[2,3,4]**, **Ho Kyeom Kim[5,6]**, **Lin Ma[1,2]** [ID], **Julian Mecklenburgh[1]**, **Roberto Rizzo[2,3]** [ID], **Mahmoud Mostafavi[5]** [ID], **Sebastian Marussi[3]**, **Robert Atwood[7]**, **Steven May[1]**, **Mohammed Azeem[3,8,9]**, **Ernie Rutter[1]**, **Kevin Taylor[1]**, and **Peter Lee[3,9]**

[1]School of Earth and Environmental Sciences, University of Manchester, Manchester, UK, [2]Manchester X-Ray Imaging Facility, School of Materials, the University of Manchester, Manchester, UK, [3]Research Complex at Harwell, Rutherford Appleton Laboratory, Didcot, UK, [4]Department of Mechanics, Materials and Civil Engineering, Ecole Centrale de Nantes, UMR CNRS UMR 6183, Nantes, France, [5]Department of Mechanical Engineering, University of Bristol, Queen's Building, Bristol, UK, [6]StressMap, The Open University, Walton Hall, Milton Keynes, UK, [7]I12 Beamline, Diamond Light Source, UK, [8]Department of Engineering, University of Leicester, Leicester, UK, [9]Department of Mechanical Engineering, University College London, London, UK

Abstract Mode-I Fracture Toughness, K_{Ic}, was measured in six shale materials using the double-torsion technique. During loading, crack propagation was imaged both using twin optical cameras, and with fast X-ray radiograph acquisition. Samples of Bowland, Haynesville, Kimmeridge, Mancos, Middlecliff, and Whitby shales were tested in a range of orientations. The measured fracture toughness values were found to be in good agreement with existing literature values. The two imaging techniques improve our understanding of local conditions around the fracture-tip, through in situ correlation of mechanical data, inelastic zone size, and fracture-tip velocity. The optical Digital Image Correlation technique proved useful as a means of determining the validity of individual experiments, by identifying experiments during which strains had developed in the two "rigid" specimen halves. Strain maps determined through Digital Image Correlation of the optical images suggest that the scale of the inelastic zone is an order of magnitude smaller than the classically used approximation suggests. This smaller damage region suggests a narrower region of enhanced permeability around artificially generated fractures in shales. The resolvable crack-tip was tracked using radiograph data and found to travel at a velocity around 470 μm/s during failure, with little variation in speed between materials and orientations. Fracture pathways in the bedding parallel orientations were observed to deviate from linearity, commonly following layer boundaries. This suggests that while a fracture traveling parallel to bedding may travel at a similar speed to a bedding perpendicular fracture, it may have a more tortuous pathway, and therefore access a larger surface area.

Plain Language Summary Fracture toughness is a measure of the strength of a material, in the presence of existing flaws or cracks. Here fracture toughness was measured in six shale materials with fractures oriented both parallel and perpendicular to the bedding layers in the shales. During the experiments, the progressing fractures were imaged using both optical cameras and radiographs recorded using a synchrotron. The radiograph images were used to track the velocity of the progressing fracture, which did not vary strongly with different materials or orientations. The optical images were used to characterize the "damage zone" around the main fracture in which microfractures develop. This region was seen to be much smaller than conventional models suggest, which could imply that the developing fractures increase permeability over a much narrower region than previously believed.

1. Introduction

Shale is the most abundant sedimentary rock in the Earth's crust, making up 50–80% of sedimentary material worldwide (Burns, 2011; Rutter et al., 2017). Shale materials are intimately entwined with hydrocarbon exploration, commonly behaving as the source rock, cap rock, or both, for conventional hydrocarbon exploration. More recently, shales have been exploited directly as a reservoir formation, using hydraulic fracturing to

increase hydrocarbon recovery from the naturally tight shale formations (Rutter et al., 2017). Fracture growth properties in shales are also of interest in the fields of CO_2 sequestration and radioactive waste disposal (Fauchille et al., 2016).

Mechanical data for these materials are therefore of great interest, especially those relating to the propagation of fractures. Fracture growth in the subsurface is often complex with tortuous pathways and significant horizontal extent (Eseme et al., 2007; Fisher & Warpinski, 2012; Khazan & Fialko, 1995; Thiercelin et al., 1989). The relationship between the materials, the loading conditions, and the intricate form of these fractures is poorly understood.

In response to these developments, the mechanical properties of shale have been the subject of many recent studies. Shale fracture toughness data specifically was sparse prior to 2015, with only a small number of studies, mostly addressing the variation of K_{Ic} with kerogen content (Chong et al., 1987; Costin, 1981; Schmidt & Huddle, 1977; Swanson, 1984; Warpinski & Smith, 1990; Young et al., 1982). More recently, a number of studies have addressed different aspects relating to K_{Ic} in shales including the effect of water saturation (Chen et al., 2017; Yang et al., 2016) and the effect of organic matter content (Kabir et al., 2017). Various theoretical studies (e.g., Garagash, 2006; Zia et al., 2018) have demonstrated that K_{Ic} becomes the dominant control on fracture propagation for conditions when the pressure gradient within a fracture has equilibrated, either due to a long timescale or a low fluid viscosity. Recent experimental studies of anisotropy and fracture deflection (Chandler et al., 2016; Forbes Inskip et al., 2018; Lee et al., 2015; Luo et al., 2018) tend to find strongly anisotropic K_{Ic} values in the region of $\simeq 0.2 - 1.5$ MPa·m$^{\frac{1}{2}}$, with much lower K_{Ic} values for fracture planes parallel to layering. This K_{Ic} anisotropy is therefore thought to be a possible mechanism for the limitation of hydraulic fracture height (Zia et al., 2018).

Linear-elastic fracture mechanics predicts a zone of inelastic deformation created by microfracturing around the tip of a progressing fracture. This inelastic zone is potentially of importance for industrial applications, as a region of microfracturing will have enhanced permeability, therefore the scale of the inelastic zone should be expected to relate to the volume of rock stimulated by a progressing fracture (Masoudian et al., 2018). The high ductility values observed during K_{Ic} experiments in shales by Young et al. (1982) and Chandler et al. (2016) suggest that the region of inelastic deformation in these materials may be large compared to that in other geomaterials, and the anisotropic K_{Ic} values measured by all authors suggest that the form of the deformation within these inelastic zones may vary as a function of orientation. Here the double-torsion method is employed specifically to investigate the scale of this inelastic zone around a progressing fracture through two complementary methods of correlative imaging. These imaging techniques allow for the strain field and fracture-tip location to be determined in relation to the applied load, thereby characterizing the inelastic zone around the progressing fracture.

The double-torsion technique is used as it features narrow plate samples, allowing for representative strains to be tracked in two dimensions. In order to image the strain field, a pair of 5 Megapixel cameras was used with the stereo optical Digital Image Correlation (DIC) technique to allow a coarse image of the strain fields of the sample surface, at a sampling frequency of 5 Hz (Sutton et al., 2009). Additionally, radiographs were acquired at a sampling frequency of 25 frames per second, in order to image the movement of the fracture-tip and crack-mouth opening displacement (CMOD) in relation to the applied load.

This approach is novel within shale materials, allowing for an improved understanding of the local conditions around a fracture as it develops. Specifically, the method presented here allows for in situ correlation of the local rock fabric with mechanical data, inelastic zone size, and fracture-tip velocity.

2. Experimental Methods

Narrow rectangular samples were loaded in the double-torsion configuration, with contemporaneous strain quantification using stereo optical DIC and fracture tracking using radiographic imaging.

2.1. The Double-Torsion Method for Fracture Toughness Determination

The double-torsion sample geometry is shown in Figure 1a. A notched thin rectangular sample is loaded from one end in a four-point bend configuration. A fracture initiates at the tip of the existing notch and then propagates over the length of the specimen. During the double-torsion experiment, the fracture front is found to be close to orthogonal to the direction of load application, with the crack propagating in mode-I
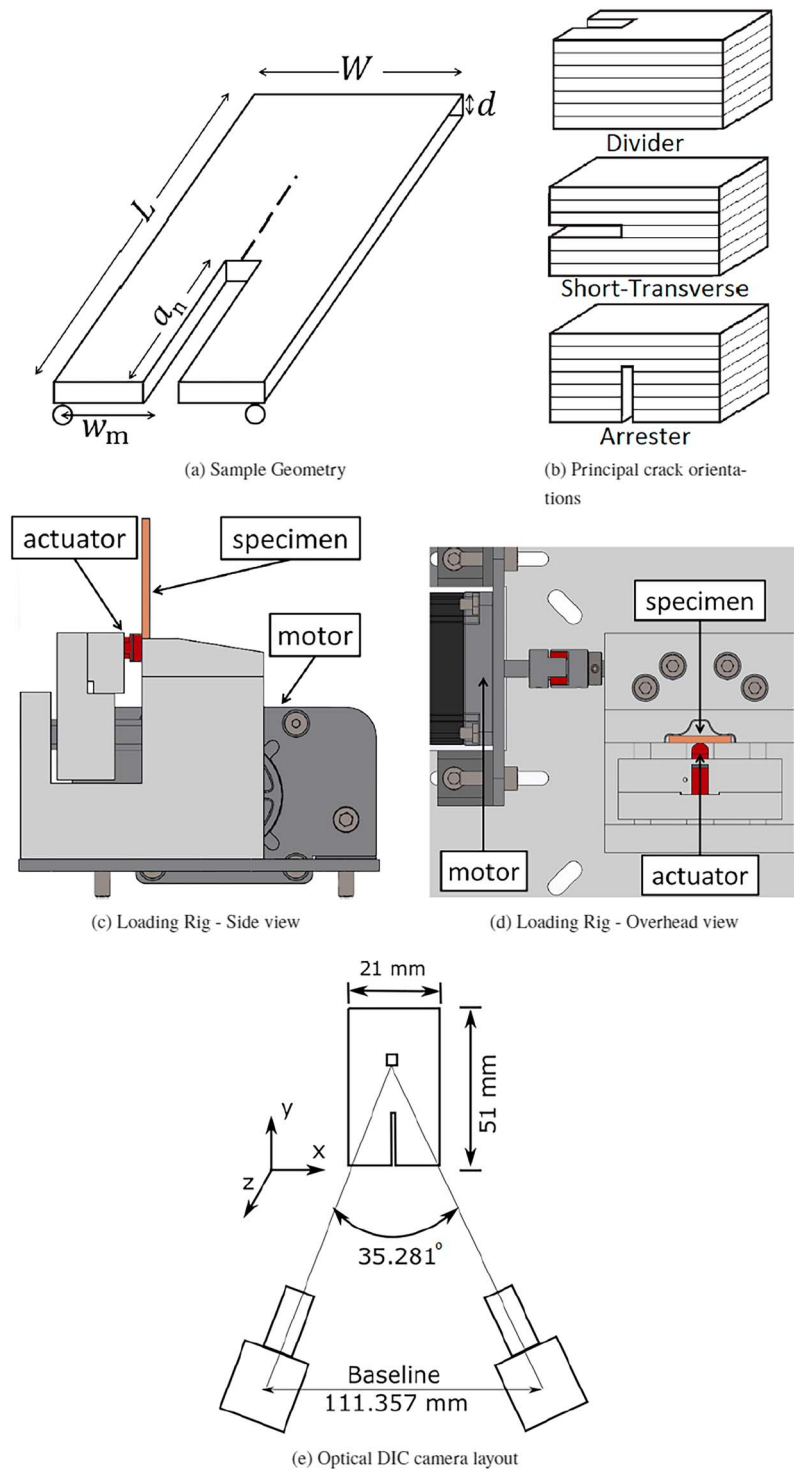
Figure 1. (a) The double-torsion specimen geometry used here. The sample dimensions used in this study are given in Table 1. Figure modified after Becker et al. (2011). (b) The three principal crack-plane orientations relative to bedding (anisotropy) planes; Divider, Short-Transverse, and Arrester. Figure modified after Chong et al. (1987). (c) and (d) profile and overhead schematics of the loading rig used here. (e) The setup of the optical DIC cameras in relation to the Double-Torsion sample. The loading ram was moved from the rear of the sample in this setup, to ensure that the maximum strain was observed on the sample surface. DIC = Digital Image Correlation.

Table 1
Nominal Sample Dimensions Used in the Experiments Described Here

Dimension	Value (mm)	Ratio to W
W	20	1
L	60	3
a_n	12.5	0.625
d	2.75	0.1375

Note. Dimensions correspond to those shown in Figure 1a. Individual sample dimensions for each test are given in the supporting information Table S1.

(Evans, 1972, 1973). The method has been the subject of a number of review papers which describe the experiment in more detail (Becker et al., 2011; Shyam & Lara-Curzio, 2006; Tait et al., 1987).

The double-torsion method is popular in the characterization of the fracture mechanics properties in brittle materials because in principle, the determined stress-intensity factor is independent of crack length. Williams and Evans (1973) showed that the strain energy release rate, G, for a mode-I crack propagating in a double-torsion specimen is given by

$$G_I = -\frac{dU}{dA} = \frac{P^2}{2d}\frac{dC}{da} = \frac{3w_m^2 P^2}{2\mu W d_n d^3 \Psi},$$ (1)

where U is total strain energy, A is fracture surface area, P is applied load, C is specimen compliance, w_m is lever arm length, μ is shear modulus, ψ is a thickness correction factor (discussed below), and d, a, W, and d_n are specimen dimensions defined in Figure 1a. An associated stress-intensity factor can be defined through

$$K_I = \sqrt{E'G},$$ (2)

where

$$E' = \begin{cases} E, & \text{(plane stress)} \\ \frac{E}{1-v^2}, & \text{(plane strain)} \end{cases}$$ (3)

Substituting equation (1) into equation (2) and using $\mu = \frac{E}{2(1+v)}$, the stress intensity is given by

$$K_I = \begin{cases} Pw_m\sqrt{\frac{3(1+v)}{Wd_n d^3 \Psi}}, & \text{(plane stress)} \\ Pw_m\sqrt{\frac{3(1+v)}{Wd_n d^3 \Psi(1-v^2)}}, & \text{(plane strain).} \end{cases}$$ (4)

The fracture toughness, K_{Ic}, can be found by setting P equal to P_{max}, the failure load. Note that from equation (4), K_{Ic} can be determined without knowing the Young's Modulus, E. Ψ is a correction factor derived by Fuller (1979), and is given by

$$\Psi(d, W) = 1 - \frac{d}{W}\left[1.2604 + 2.400e^{\left(\frac{-W\pi}{2d}\right)}\right].$$ (5)

It accounts for the interaction between the two surfaces and becomes significant when $d/W > 0.15$ (Tait et al., 1987). Due to the roughness of the fracture surfaces generated in shale materials, we might expect the Ψ found here to be a minimum value, as interaction between the fracture faces is likely to be larger than in most engineering materials due to the tortuosity expected in the fracture path.

Four main assumptions are involved in the derivation of these expressions, as described by Becker et al. (2011).

1. The fracture is assumed to propagate purely in mode-I (opening).
2. The sample is assumed to behave as if it is made up of two symmetric and independent halves. These halves only experience the load, P, with the lever arm length, w_m.
3. The unbroken ligament in front of the crack-tip is assumed to remain rigid.
4. The crack profile is assumed to remain constant throughout propagation.

It can be seen from the right hand side of equation (1) that the energy release rate, G, (and therefore, the stress-intensity factor, through equation (2) is not dependent on a, and therefore, the stress intensity experienced at the crack-tip is independent of fracture length. This property implies that the propagation of the fracture can be controlled, as all variables on the right hand side of equation (1) will remain constant during the experiment, with the exception of the load, P. Therefore, during a double-torsion experiment, the stress intensity at the crack-tip should vary purely according to the square of the applied load, $K_I \propto P^2$. In conventional fracture mechanics notation then, $\frac{\delta Y^*}{\delta a} = 0$ for double-torsion experiments, where $K_I = Y^* \sigma \sqrt{\pi a}$.

2.2. Principal Crack Orientations in a Transversely Isotropic Material

Shales commonly exhibit transverse isotropy in terms of their elastic and mechanical properties. In transversely isotropic media, we can define three principal crack orientations with respect to the anisotropy (bedding) plane, as described by Schmidt and Huddle (1977) and Chong et al. (1987). The principal orientations are known as Divider, Short-Transverse, and Arrester, respectively, and are illustrated in Figure 1d.

In the Divider orientation, the crack plane is normal to the isotropy (bedding) plane but the crack propagates in a direction parallel to the isotropy plane. In the Short-Transverse orientation both the crack plane and the crack propagation direction are parallel to the isotropy plane. Finally, in the Arrester orientation, both the crack plane and the crack propagation direction are normal to the isotropy plane. For a horizontally bedded material, the Divider, Short-Transverse, and Arrester orientations correspond, respectively, to a vertically oriented fracture propagating horizontally, a horizontal fracture propagating horizontally, and a vertically propagating fracture (Chandler et al., 2016).

The inclined nature of the fracture-tip within the double-torsion specimen does not affect the orientation of the developing fracture in the short-transverse orientation. However, for samples manufactured in the Arrester or Divider orientations, fractures will actually propagate at an intermediate angle between the Arrester and Divider orientations.

### 2.3. Sample Geometry and Manufacture

The double-torsion sample geometry is shown in Figure 1a. The approximate dimensions used in the experiments described here are listed in Table 1, but there is significant variation in the sample dimensions due to the difficulty of producing thin slices of shale. These nominal dimensions correspond approximately to a geometry, $(W : L : d : a_n)$ of (1:3:0.1375:0.625). These samples are slightly thicker than the dimensions recommended by Becker et al. (2011), and the stress intensities should therefore be expected to display some small crack-length dependence. The ratio $\frac{d}{W} = 0.1375$, is lower than the threshold of 0.15 above which the correction factor, $\Psi(d, W)$, becomes significant (Tait et al., 1987).

It is commonplace in double-torsion experiments to use a central groove running the whole length of the sample (i.e., $d_n < d$, for some central region, $W_{groove} \ll W$; Tait et al., 1987). This groove acts to keep the fracture running centrally through the sample, because from equations (1) to (2) it can be seen that $K_I \propto d^{-2}$, hence a very large stress concentration is generated. Consequently, the fracture is strongly incentivized to remain within the grooved region. No such central groove was used in the experiments presented here, because part of the experimental goal was to observe the effect of the material anisotropy and inhomogeneity on crack-path trajectory under (nominally) mode-I loading.

Sample manufacture varied slightly between different materials and orientations. In most cases, a block with end dimensions $W \times L$ was cut using a slow-rotating circular saw. A central notch of length a_n was then cut into the center of the narrow side using a smaller saw. This left a notch width of around 1 mm. The notched block was then sliced into samples of thickness, d. Due to low availability and irregular shape of some of the materials tested, other samples were manufactured in a less formulaic fashion, with slices simply cut where possible and notched appropriately. There are therefore significant discrepancies in the numbers of samples between different materials and orientations. In particular, sample manufacture in the arrester orientation proved to be very difficult, with the "legs" to either side of the notch commonly breaking off once the notch had been cut.

2.4. Experimental Equipment and Setup

The double-torsion samples were loaded using the frame shown in Figures 1c and 1d. This loading frame was adapted for use with correlative X-ray and optical DIC. The sample is mounted vertically, against two rods of 2 mm diameter and 10 mm height, separated by 5 mm on one side. On the other side, a central actuator with a 2 mm diameter semicylindrical contact area moves horizontally toward the sample. This semicylindrical form
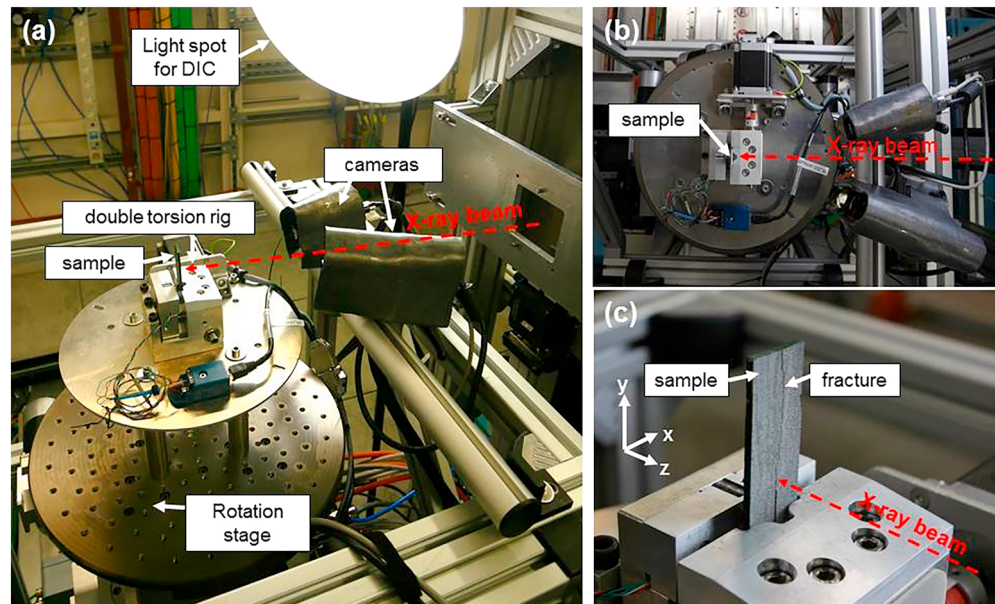
Figure 2. Photographs showing the setup of the double-torsion rig and optical cameras relative to the rotations stage and X-Ray beam within experiment hutch on beamline I12 at Diamond light source. (a) Double-torsion rig on rotation stage. (b) Overhead view of rotation stage. (c) Close-up of double-torsion loading rig. DIC = Digital Image Correlation.

acts to keep the sample aligned centrally during loading. The two loading point contacts are provided by the points where the semicylinder makes contact with the two sides of the notch. The actuator was driven at 2 μm/s by a stepper motor under displacement rate control. Figure 2 shows photographs of the setup of these pieces of equipment in relation to one another.

2.5. Strain Determination Using Optical DIC

Two Dantec 3-D DIC cameras were mounted facing the double-torsion sample at angles allowing for ≃35° separation. This setup is shown in Figure 1e. Two CCD cameras with 35 mm focal length lenses were used. The cameras face the opposite side of the sample to the loading actuator, which ensures that the images are taken from the side of the sample where the maximum strain should be expected. External LED lights were used for illumination. The 8-bit images of $2,448 \times 2,050$ pixels were acquired every 0.2 s. The field of view was 36.72×30.75 mm which correspond to a spatial resolution of approximately 15 μm/pixel. Theoretically, DIC can resolve at 0.01 pixel accuracy based on the subpixel resolution algorithms in optimum experimental conditions (Pan et al., 2009). However, this cannot be achieved in practice due to the uncertainties caused by experimental sources such as speckle quality, camera motion, and lighting conditions (Reu, 2012a). Therefore, in this experiment, the displacement accuracy was assumed between 0.15 and 0.3 μm/pixel, corresponding to 0.01 and 0.02 of estimated subpixel resolution accuracy.

The accuracy of the DIC system depends heavily on the quality of a distinguishable speckle pattern on the sample surface. Reu (2012b) recommends that a random uniform speckle pattern with a speckle size of $3 - 5$

Table 2
Summary of the Materials Used in the Double-Torsion experiments

Material	Microstructure	Mineralogy	TOC	Maturity	Porosity
Bowland shale	Non-laminated	Quartz/Carbonate rich	Medium	Oil mature	Unknown
Haynesville shale	Laminated	Clay rich	High	Gas mature	7%
Kimmeridge shale	Laminated	Clay rich	High	Oil mature	7%
Mancos shale	Laminated	Quartz rich	Medium	Immature-Oil mature	9%
Middlecliff shale	Laminated	Clay rich	Unknown	Unknown	Unknown
Whitby mudrock	Non-laminated	Clay rich	Medium	Immature	8%
Pennant sandstone	Non-laminated	Quartz rich	Zero	N/A	5%
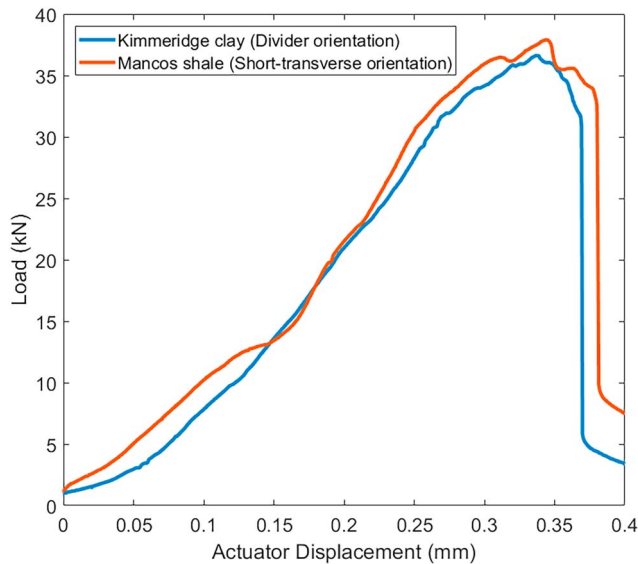
Figure 3. Example plots of load as a function of actuator displacement for a Divider orientation sample of Kimmeridge clay and a Short-Transverse orientation sample of Mancos shale.

pixel is applied to a sample surface. Here such a speckle pattern was created on the sample surface, using matt black and white spray paint in order to generate an artificial texture to be tracked by the DIC. The strain was calculated by taking the gradient of two adjacent subsets of displacement data. Each subset is a region within which the strain value is calculated by averaging the strain values therein (Reu, 2012c). A larger subset size will reduce noise in the strain, but at the expense of spatial resolution. In this experiment, subset and step sizes of 25 and 19 pixels were used, respectively, to generate the strain fields and found to be most effective.

2.6. Radiograph Imaging of Crack Propagation

Time-resolved radiograph imaging of the progressing fracture was conducted using experiment hutch 1 on the I12 beamline at Diamond Light Source, Harwell, UK, during beamtime EE13824. The synchrotron beam energy was maintained at 20 keV. A $2{,}048 \times 2{,}048$ pixel image was recorded 25 times every second using a PCO.edge camera with 2X magnification. The temperature was kept constant at 20 °C, and relative humidity was maintained at 50%. Dark field and reference field images were recorded at the start and end of each experiment.

3. Sample Materials

Six different shales were tested to provide mechanical properties for as broad a range of materials as possible. Additionally, Pennant sandstone was tested. As a low permeability, quartz-rich sandstone, it is used as a tight-gas sandstone analog, and so has relevance for hydraulic fracture propagation. It was deemed to be important to perform the double-torsion experiment on at least one nonshale material, so as to provide a benchmark with which to compare the behavior of the shale. All experiments were conducted on samples that had been dried in an oven at 60 °C until reaching a constant mass.

Due to sample scarcity and difficulties in sample manufacture, sample numbers vary significantly between different orientations and materials. In particular, samples proved very difficult to manufacture in the Arrester orientation. The properties of the materials tested here are summarized in Table 2.

Table 3
Mean K_{Ic} Values for the Materials Tested Here

Material	Orientation	K_{Ic}(Plane Stress) $(MPa \cdot m^{1/2})$	K_{Ic}(Plane Strain) $(MPa \cdot m^{1/2})$	n (experiments)
Mancos shale	Divider	0.47 ± 0.15	0.48 ± 0.15	6
Mancos shale	Short-Transverse	0.36 ± 0.18	0.37 ± 0.18	6
Mancos shale	45°	0.30	0.30	1
Whitby mudrock	Divider	0.36 ± 0.22	$0.37 \pm m0.23$	6
Whitby mudrock	Short-Transverse	0.06	0.06	1
Bowland shale (PH-1)	Arrester	0.91 ± 0.12	0.93 ± 0.13	5
Bowland shale (PH-2)	Short-Transverse	0.35	0.35	1
Haynesville shale	Divider	0.37 ± 0.14	0.38 ± 0.15	3
Kimmeridge shale	Divider	0.47 ± 0.15	0.48 ± 0.16	6
Kimmeridge shale	Short-Transverse	0.08	0.09	1
Middlecliff shale	Divider	0.29 ± 0.18	0.29 ± 0.18	4
Pennant sandstone	Divider	0.32 ± 0.12	0.33 ± 0.13	17
Pennant sandstone	Short-Transverse	0.32 ± 0.06	0.32 ± 0.06	9

Note. In each case, the uncertainty is given by the standard deviation of n (experiments). We expect that the crack-tip should be close to plane strain conditions and include the plane stress values only for completeness. For samples manufactured in the Arrester or Divider orientation, the K_{Ic} values should be considered to be at an intermediate angle between the two orientations, as described in section 2.2.
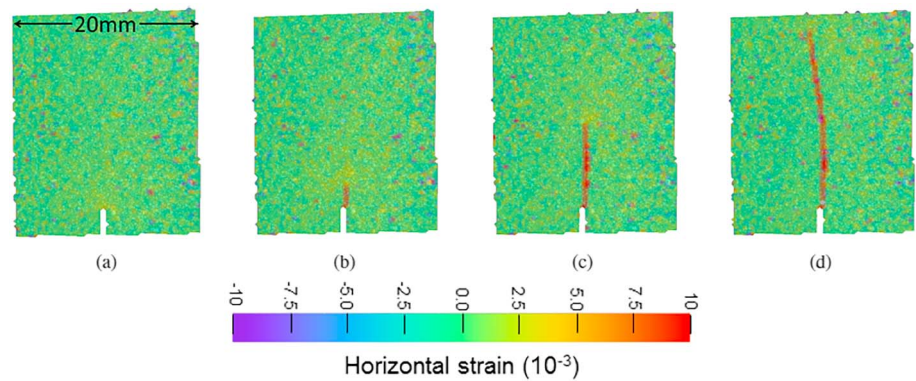
Figure 4. Horizontal strains (corresponding to the *x*-orientation in Figure 2c) recorded using optical Digital Image Correlation during the loading of a sample of Kimmeridge clay in the Divider orientation. (a) shows the sample before any loading is applied and (d) shows the sample after peak load. (b) and (c) show the fracture at intermediate times.

Bowland shale is a carboniferous organic-rich basinal marine shale found across the North-West of England (Andrews, 2013). The samples used here were taken from core material from the Preese Hall 1 borehole, as used by Fauchille et al. (2017).

Haynesville- Bossier shale is an organic-rich Jurassic mudstone found in Texas and Louisiana (Hammes & Frébourg, 2012). It is one of the largest and most active hydrocarbon-producing reservoirs in the United States. The sample selected here is from the dominant fine mudstone microfacies in the Haynesville-Bossier Shale and was taken from the same core as was used by Dowey and Taylor (2017) and Ma et al. (2018).

Kimmeridge shale is a silt-bearing clay-rich Jurassic mudstone and is the major source rock for North Sea oil. The samples used here were taken from the same blocks as those used by Hawthorn (2004) and were sourced from an oil well in the central North Sea.

Mancos shale is found in the Rocky Mountain area of western Colorado and eastern Utah and provides the source for many of the shale plays in the Rockies (Longman & Koepsell, 2005). It is a strongly laminated Upper Cretaceous shale deposited 90 – 70 Ma (Chidsey & Morgan, 2010). The samples used here were taken from the same block as those used by Chandler et al. (2016, 2017).

Middlecliff shale is a Lower Westphalian lower coal-measure mudstone found in northern England (Ashby & Pearson, 1979). It is strongly laminated and very friable.
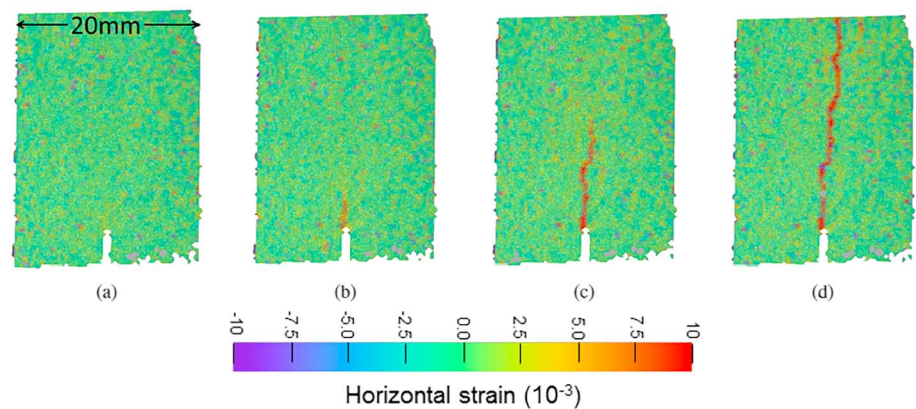
Figure 5. Horizontal strains (corresponding to the *x*-orientation in Figure 2c) recorded using optical Digital Image Correlation during the loading of a sample of Mancos shale in the Short-Transverse orientation. (a) shows the sample before any loading is applied and (d) shows the sample after peak load. (b) and (c) show the fracture at intermediate times.
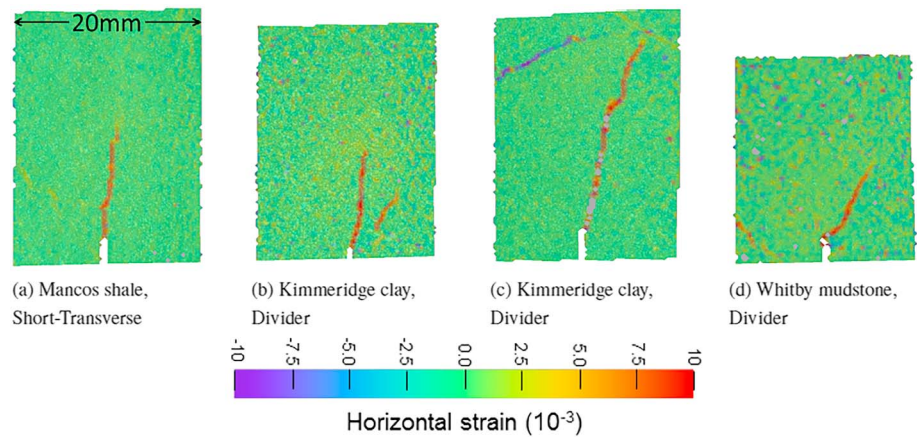
Figure 6. Final horizontal strains (corresponding to the *x*-orientation in Figure 2c) after sample failure recorded using optical Digital Image Correlation during the loading of various samples, demonstrating fracture deflections. The stresses calculated from the loading of these samples were not used to determine fracture toughness values. (a) Mancos shale, Short-transverse; (b) Kimmeridge clay, Divider; (c) Kimmeridge clay, Divider; (d) Whitby mudstone, Divider.

Whitby Mudstone is found on the North-East coast of England, and forms part of the Lias Group, made up of early Jurassic siliciclastic mudstones deposited in the Cleveland Basin (Rawson & Wright, 1995). The samples used here were taken from the same block as those used by McKernan et al. (2014, 2017), who describe it as a bioturbated silt-bearing, clay-rich mudstone.

Pennant sandstone is a quartz sandstone deposited in South Wales during the Upper Carboniferous (Kelling, 1974). The samples used here were taken from the same block as used by Hackston and Rutter (2016), who used Scanning Electron Microscopy (SEM) chemical mapping to find a composition of 70% sutured quartz grains and 15% feldspar with the interstitial space containing clusters of muscovite, oxides, and clay minerals.
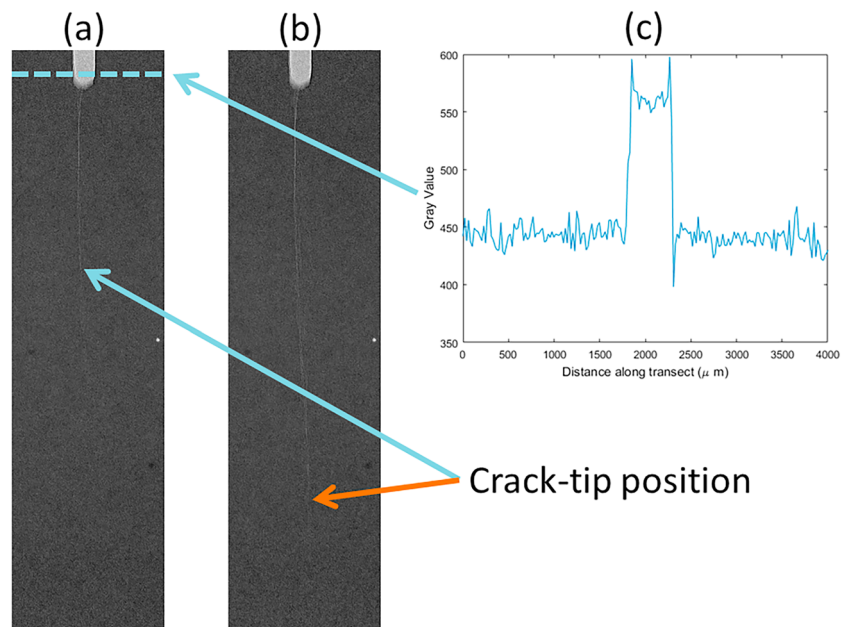
Figure 7. (a, b) Examples of radiographs from sample KIMdiv7, after ≃140 and ≃170 s, respectively, demonstrating where the crack-tip was picked. (c) Example grayscale transect corresponding to (a), used for Crack-Mouth Opening Displacement picking. In this case, Crack-Mouth Opening Displacement ≃ 500 μm.

4. Results

Figure 3 shows example curves of the load, P, as a function of the actuator displacement, x. In each case the load is observed to increase linearly with applied actuator displacement, before breaking abruptly at the failure load as the crack reaches the end of the sample.

Table 3 lists the mean fracture toughness values measured for each of the materials tested here. The n(tests) varies significantly between the different materials and orientations due to a combination of the material availability and the difficulty in manufacturing samples in certain orientations as described in section 2.3. Four K_{Ic} values are listed for each material, calculated assuming that the crack-tip is in plane stress and plane strain, using Evans' conventional method (equation (4)) . We expect that the crack-tip should be close to plane strain conditions, and include the plane stress values only for completeness.

Mean fracture toughness values were calculated from the failure loads, P_{max} , and sample dimensions of all experiments in which the fracture was not observed to deviate from the central axis by more than 3 mm while propagating through the central third of the sample length. Fracture deflection was quite common-place due to the anisotropy and heterogeneity of the material, and the lack of a central sample groove (as described in section 2.3). These fracture deflections are not discussed here, but are intended to form part of a later publication.

4.1. Surface Strains Determined Through Optical DIC

Horizontal strain fields determined using the optical DIC equipment described in section 2.5 were processed using Istra 4-D software. Significantly more random noise is visible in the strain maps than was the case during calibrations. This noise is believed to be caused by the scattering of the X-rays used for the radiography. Figure 4 shows horizontal strain maps calculated at four instances throughout the loading of a Divider orientation sample of Kimmeridge clay. The strain map clearly shows the opening of the fracture, which grows in the intended vertical direction, from the notch-tip.

Figure 5 shows horizontal strain maps calculated at four instances throughout the loading of a Short-Transverse orientation sample of Mancos shale. Despite being in the Short-Transverse orientation, the fracture is seen to be much less straight, due to the inhomogeneity in the Mancos shale.

Figure 6 shows horizontal strain maps immediately prior to complete failure for four different samples in which the fracture was judged not to be suitable to calculate K_{Ic} directly from the load record. In some cases this corresponds to a fracture which deflects sharply from the intended propagation direction, but in other cases (such as Figure 6b), the DIC measurements demonstrate that these experiments feature strains developing away from the main notch. This provides an additional form of quality control on the fracture toughness measurements, as the deformation in the side regions of these samples violates the second of the assumptions described in section 2.1 but this deformation was not apparent from visual inspection of the sample.

4.2. Crack-Tip Position and CMOD Determined from Radiograph Images

Crack-tip position was picked manually from the radiographs after the dark and reference field corrections had been made. Figures 7a and 7b show example radiographs as the fracture propagates across a Divider orientation sample of Kimmeridge shale, demonstrating where the crack-tip was picked from local changes in the grayscale value. The position of the crack was manually tracked every 20 frames (0.8 s) using the Manual Tracking plug-in in Fiji image processing software (Schindelin et al., 2012).

CMOD was picked using a grayscale transect in a direction perpendicular to the notch as shown in Figure 7c. The boundaries of the crack mouth were picked as the points at the base of the rise, in each case.

5. Discussion

5.1. Comparison With Previous Experimental Fracture Toughness Data in Shale

Shale fracture toughness data were sparse in the scientific literature prior to 2015, and only one study considered measurements in more than one orientation. Schmidt and Huddle (1977) used three-point bend specimens to measure K_{Ic} values varying from 0.3 to 1.1 MPa·m$^{\frac{1}{2}}$ for two grades of Anvil Points oil shale across the three principal crack orientations. They found that increased hydrocarbon content produced lower fracture toughness measurements, and that in both cases the Divider orientation has the highest and the Short-Transverse orientation the lowest K_{Ic} value. Chong et al. (1987) summarized their own results and those of Costin (1981) and Young et al. (1982) on oil shales in the Divider orientation, finding K_{Ic} in the range 0.6 – 1.1

MPa·m$^{\frac{1}{2}}$, but demonstrating the opposite trend, with fracture toughness and ductility increasing with hydrocarbon content. Warpinski and Smith (1990) quote $K_{Ic} = 1.43$ MPa·m$^{\frac{1}{2}}$ for the Mancos shale, but do not describe the method or orientation used.

More recently, a number of groups have addressed fracture toughness measurement in shales, with studies by Lee et al. (2015), Chandler et al. (2016, 2017), Chen et al. (2017), Kabir et al. (2017), Luo et al. (2018), and Forbes Inskip et al. (2018). Lee et al. (2015) used semicircular bend specimens to measure fracture toughness in the Divider and Arrester orientations in the Marcellus shale, as well as at an angle of 30° to the Arrester orientation. They found fracture toughness of K_{Ic} values varying between $\simeq 0.2$ and 0.7 MPa·m$^{\frac{1}{2}}$, with the off-axis measurement the weakest and the Arrester orientation the strongest. Chandler et al. (2016) used short-rod experiments to measure the fracture toughness of Mancos shale in the three principal crack orientations. Yang et al. (2016) used a method based on nanoindentation to investigate the effects of hydrophobic coatings and water saturation on samples of Sichuan gas shale. They found the hydrophobic coating to increase K_{Ic}, and increase in water saturation to decrease K_{Ic}. They obtained a fracture toughness of 2.7 Mpa.m$^{\frac{1}{2}}$ for their untreated, air-dried sample. Kabir et al. (2017) used microscopic scratch tests to measure the fracture toughness of Toarcian gray shale and Niobrara black shale, and found that their fracture toughness values vary as a function of scratch speed, reaching an intrinsic value at high scratch speeds. The intrinsic fracture toughness values that they measured are much higher than those measured by other authors, on the order of $\simeq 4.0-5.5$ Mpa.m$^{\frac{1}{2}}$. Even at the slowest scratch speeds that they test, they found fracture toughnesses in the region of 2 Mpa.m$^{\frac{1}{2}}$. Luo et al. (2018) and Forbes Inskip et al. (2018) each used bend specimens to investigate the variation of K_{Ic} in the Arrester, Short-Transverse, and Divider orientations, as well as at angles between the Arrester and Short-Transverse orientations. Luo et al. (2018) investigated the Chongqing shale, and found K_{Ic} to vary in the $\simeq 0.9-1.6$ Mpa.m$^{\frac{1}{2}}$ range. Forbes Inskip et al. (2018) investigated Nash Point shale, and found K_{Ic} to vary in the $\simeq 0.2-0.7$ Mpa.m$^{\frac{1}{2}}$ range, with the short-transverse orientation the weakest and the Arrester and Divider orientations comparable.

To date, two studies have looked at double-torsion experiments in shale materials. Swanson (1984) conducted double-torsion experiments on a Devonian shale, finding subcritical crack growth behaved similarly in the shale as in Westerly granite and three different Basalts. Chen et al. (2017) conducted stress relaxation double-torsion experiments on Woodford shale with the material in varying saturation states. They found a fracture toughness of 0.76 Mpa.m$^{\frac{1}{2}}$ for unsaturated states and a strong water-weakening effect. Their samples were manufactured in the Divider orientation, so that the fracture front lies between the Divider and Arrester orientations.

The shale fracture toughness values listed in Table 3 are generally in the same range as those discussed by Schmidt and Huddle (1977), Chong et al. (1987), Lee et al. (2015), Chandler et al. (2016), Chen et al. (2017), Luo et al. (2018), and Forbes Inskip et al. (2018; summarized in section 1), varying between $\simeq 0.25$ and 1 MPa·m$^{\frac{1}{2}}$. In all materials where multiple orientations were tested, the same trend is observed as by Schmidt and Huddle (1977), Lee et al. (2015), Chandler et al. (2016), and Forbes Inskip et al. (2018), with the K_{Ic} highest in the Arrester orientation and lowest in the Short-Transverse orientation. The Divider and Short-Transverse orientation measurements on the Mancos shale show very good agreement with the K_{Ic} values measured by Chandler et al. (2016) using the short-rod method on the same material. Pennant sandstone is seen to be isotropic in K_{Ic}.

The fracture toughness values found here are significantly lower than the ranges reported by Yang et al. (2016) and Kabir et al. (2017). Kabir et al. (2017) described their Niobrara shale sample as demonstrating exceptional toughness and suggested that this is due to toughening mechanisms in the kerogen, and kerogen-clay interfaces. However, while their Niobrara shale sample is very kerogen-rich and quartz-poor, their Toarcian shale and the Sichuan shale sample used by Yang et al. (2016) also display K_{Ic} values around four times higher than those measured by other authors, yet do not feature exceptional kerogen content. It is tempting to consider that the much smaller experimental scale of these two studies may contribute to this discrepancy, to some extent. In compressive strength measurement, smaller-scale experiments have been shown to record higher strengths in a range of materials. In particular, recent micropillar compression experiments conducted by Keller et al. (2017) demonstrate a compressive strength three to four times higher at the microscale in Opalinus clay as is found at the macroscale by Giger and Marschall (2014). Smaller samples can contain a smaller maximum-flaw size, and the largest stress concentrations should occur at the tips of the largest flaws, meaning that larger samples can fail at lower stresses. While this explanation makes sense for compressive strength experiments, it is more difficult to explain in fracture toughness experiments such as those described

Table 4
Tensile Strength, Young's Modulus, Failure Strain, Yield Radius, and Critical Radius for Mancos Shale, Whitby Mudstone, and Pennant Sandstone

Material	Orientation	σ_T (MPa)	E (MPa)	$\epsilon_T (\simeq \epsilon_Y)$ (%)	r_Y (mm)	r_c (mm)
Mancos shale	Divider	5.81	24,800	0.023	0.030	1.1
Mancos shale	Short-Transverse	4.54–7.35	24,800	0.018–0.030	0.038	0.4–1.1
Mancos shale	Arrester	7.28	24,800	0.029	0.038	0.3
Whitby mudstone	Divider	3.21	12,600	0.025	0.030	2.1
Whitby mudstone	Short-Transverse	2.86	12,600	0.022	0.023	0.1
Whitby mudstone	Arrester	4.61	8,400	0.054[a]	0.038	1.0
Pennant sandstone	Divider	15.1	23,600	0.063	0.030	0.071

Note. The measured r_Y values are in the region of 5 pixels, so have a very large associated uncertainty, and should only really be interpreted as an order of magnitude. The σ_T and E are taken from Chandler et al. (2016) for Mancos shale. Brazilian disk experiments were conducted on Whitby mudstone and Pennant sandstone here, with example load curves shown in Figure S1. In each case, E is an average determined for all orientations in the material.
[a] K_{Ic} in the Arrester orientation was assumed to be equal to the value in the divider orientation, because it was not measured here.

here. Here the largest flaw in the sample is controlled during sample manufacture, with the notch playing the role of an artificial flaw. Therefore, this argument does not explain the factor of $\simeq 4$ difference between the nanoscale/microscale measurements of Yang et al. (2016) and Kabir et al. (2017) and the macroscale measurements in the literature.

5.2. Scale of the Inelastic Zone Around the Fracture-Tip

For each experiment, K_{Ic} was calculated using equation (4). In each case, the K_{Ic} value calculated assuming that the crack-tip is in plane strain is slightly higher than that calculated assuming plane stress, by a factor of $[1/(1 - v^2)]^{\frac{1}{2}}$. The effect is, however, very small, with the difference lying within experimental uncertainty for most materials tested here.

If the size of the inelastic process zone is not negligible relative to the sample size, then yielding at the crack-tip is not completely suppressed as would be the case in true plane strain conditions (Rice, 1974). If this is the case for our samples, then our calculated K_{Ic} values will be overestimated (Wang & Pilliar, 1989). The fact that the Mancos shale values found here are approximately 1.15 times that measured by Chandler et al. (2016) could therefore suggest that the sample size used here is still in the range where measured fracture toughness displays some sample-size dependence, but the difference is very small.

5.2.1. Evolution of the Scale of the Inelastic Zone

The yield strain, ϵ_Y, of each material was estimated using

$$\epsilon_Y = \frac{\sigma_Y}{E}, \tag{6}$$

where σ_Y is the yield stress and E is Young's modulus. Table 4 lists ϵ_Y, σ_Y, and E for each material, as well as the method used to determine each value. Chandler et al. (2016) observe negligible yielding in the load versus displacement curves for Brazilian disk experiments in Mancos shale, and we observe the same here in Brazilian disk experiments on Whitby mudstone and Pennant sandstone (see supporting information). Therefore, here we take $\sigma_Y \simeq \sigma_T$, where σ_T is the tensile strength. The ϵ_Y values should therefore be thought of as maximum bounds. Once ϵ_Y had been calculated, an approximate radius of the yielding region, r_Y, was found by taking half of the median width of the region where $\epsilon > \epsilon_Y$ from representative strain fields such as those displayed in Figures 4–6. Due to the ϵ_Y values being maximum bounds, the r_Y values should be thought of as minimum bounds, although the difference should be small. The r_Y values for Mancos shale, Whitby mudstone, and Pennant sandstone are listed in Table 4. Neither σ_Y or σ_T was found in the literature for the other materials tested here, and so r_Y could be calculated. The r_Y is found to be in the region of $\simeq 0.04$ mm for each material and orientation. These r_Y values correspond to approximately 2–4 pixels in the strain fields, so should be thought of as nothing more than order of magnitude estimates.

Schmidt (1980) proposed a model based around the maximum normal stress criterion, for the estimation of r_c, the critical radius. The r_c is commonly considered to mark the radius of a circular fracture process zone

around the crack-tip (Ayatollahi & Aliha, 2008; Janssen et al., 2002; McClintock & Irwin, 1965). According to the Schmidt (1980) criterion,

$$r_c = \frac{1}{2\pi} \left(\frac{K_{Ic}}{\sigma_T} \right)^2 . \tag{7}$$

The r_c values for Mancos shale, Whitby mudstone, and Pennant sandstone are listed alongside the r_Y values in Table 4. Fracture critical radii, r_c, are found to be on the order of 1 mm for cracks propagating in the Arrester or Divider orientations in the shales, but an order of magnitude smaller in the sandstone and in the Short-Transverse orientation in the shale. These values are each 1–2 orders of magnitude higher than the yield radii, r_Y, except in the case of Pennant sandstone. This suggests that the critical radius approximation proposed by Schmidt, is perhaps overestimating the region of inelastic deformation in shale materials while remaining appropriate in the more brittle Pennant sandstone material. If these smaller zones of inelastic deformation in shale are accurate, then the region of increased permeability around a fracture within a shale may be an order of magnitude smaller than is expected from the model of Schmidt (1980).

5.2.2. Validity of the Small-Scale Yielding Criterion

The small-scale yielding criterion is the assumption that the zone of inelastic deformation around the crack-tip is small in comparison to the total volume of the sample (Janssen et al., 2002). Here we see that while the scale of the yielding zone (defined either through r_Y or r_c) is small relative to the loading direction, r_c is a significant proportion ($\simeq \frac{1}{3}$) of the sample thickness. However, the fracture-tip has been shown to be steeply inclined in double-torsion specimens, making a small angle with respect to the x-y plane (Evans, 1973). This implies that the double-torsion specimen thickness is in the direction of fracture propagation, and therefore the sample length is the dimension that corresponds to the plate-thickness for determining whether the sample is in plane strain.

There is good agreement between K_{Ic} measured here in the Mancos shale and that measured by Chandler et al. (2016), with the values measured here slightly higher. This small difference is perhaps surprising, because of the difference in scale between the large 60 mm cores tested in the former study and the much smaller samples tested here. Chandler et al. (2016) used such large cores so as to ensure the validity of the small-scale yielding criteria.

The agreement between the K_{Ic} values measured here and by Chandler et al. (2016) could therefore be seen as supporting the far smaller inelastic zone suggested by r_Y, which would correspond to a much smaller proportion ($\simeq \frac{1}{100}$) of the sample thickness. In such a case, both the experiments conducted here and those conducted by Chandler et al. (2016) could satisfy the small-scale yielding criterion, and therefore K_{Ic} would be scale-invariant, hence the agreement.

### 5.3. Validity of the Williams and Evans (1973) Method in Shale Materials

In section 2.1, four assumptions that are made in the derivation of the stress-intensity factor are described. The heterogeneity and anisotropy of the shale materials tested here are likely to cause greater violation of these assumptions than would occur in relatively isotropic and homogeneous materials. In particular, if the millimetric-scale bedding planes in the material do not lie perfectly parallel to one another, small mode-II displacement components are induced as the fracture propagates from one bed into the next, breaking assumption 1. This effect is expected to be particularly large in the Arrester orientation, where many bedding interfaces will be crossed. Additionally the fracture faces in the shale materials were seen to be quite rough. This is likely to violate assumptions 2 and 4, as some friction will be generated by contact between the surfaces of the newly formed fracture. The load required to generate a given stress intensity at the notch-tip should then be expected to increase, and therefore our fracture toughness values should be thought of as maximum values within a range.

From section 5.2, the region of inelastic deformation around the fracture-tip is seen to be small, and no significant yielding ahead of the fracture is observed in Figures 4–6. Therefore, the region ahead of the progressing fracture does appear to remain rigid and accordingly, accordingly assumption 3 seems valid.

Figure 6b shows an example of an experiment during which strain accumulates in a region not directly connected to the main fracture. In this case, assumption 2 is violated as the two halves of the sample are not behaving as rigid bodies. The small feature accumulating strain was not clearly visible on the sample surface itself, during or after the experiment. This suggests that optical DIC can provide a valuable form of quality
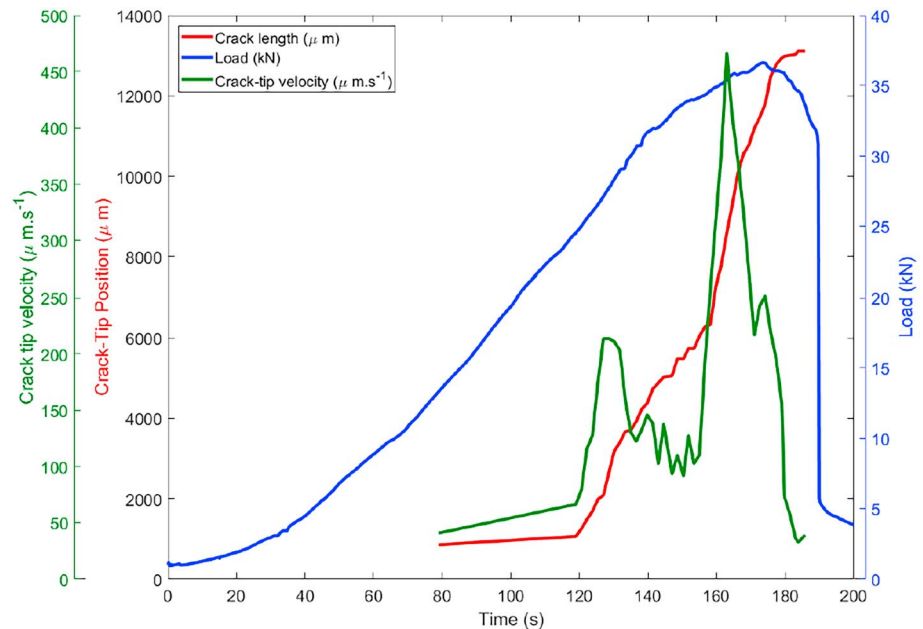
(a) Kimmeridge clay, Divider
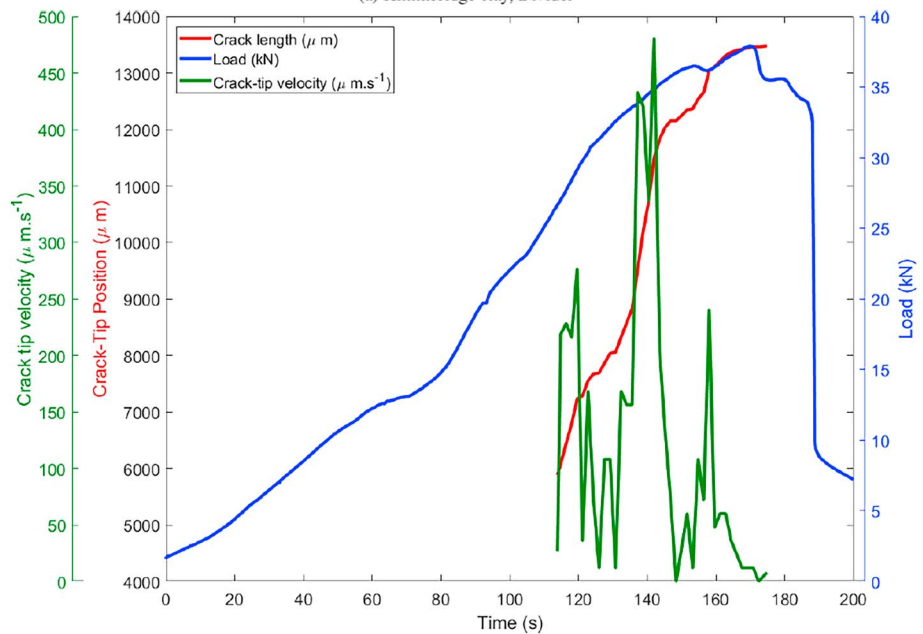
(b) Mancos shale, Short-Transverse

Figure 8. Crack-tip position, velocity, and load as a function of time for a Divider orientation sample of Kimmeridge clay (a), and a Short-Transverse orientation sample of Mancos shale (b). Crack-tip position and velocity are measured exclusively in the y direction as defined in Figure 2. The velocity data has a 5-point moving average filter applied.

control for ruling out this type of off-plane deformation during mechanical experiments in these semibrittle materials.

5.4. CMOD and Crack-Tip Velocity Determined From Radiograph Images

CMOD was calculated from the radiograph images by taking a transect of the grayscale at the tip of the initial notch and monitoring the width of the high-grayscale region. Crack-tip location was picked manually using both the raw radiograph images and difference maps of the current radiograph with the radiograph of the undeformed sample subtracted. It is important to note that while the resolution of CMOD is controlled by the image resolution of 20.8 μm, the form of the specimen means that while the crack-tip is loaded in mode-I, the surfaces of the initial notch are actually subject to rotation relative to the plane of the radiographs. This causes

the CMOD data to be very noisy. The crack-tip velocity calculated here corresponds only to the velocity of the *resolvable* crack-tip (i.e., the point along a crack's length where it the crack aperture is greater than the pixel size). The relationship between the *true* and resolvable crack-tip velocity is not known.

Figure 8 shows crack-tip *y* position, velocity ($\frac{dy}{dt}$), and load as a function of time for a Divider orientation sample of Kimmeridge clay, and a Short-Transverse orientation sample of Mancos shale. CMOD was extremely noisy and was not observed to change by more than 2 pixels, therefore it is not plotted here.

In each case, the crack-tip only became visible once the load had reached approximately 20 kN. Prior to this load, the crack had either not yet initiated, or was too narrow to resolve. In each case velocity initially rose steeply to approximately 250 μm/s during the linear portion of the loading curve. The crack-tip velocity was then seen to drop sharply and plateau during the period as the load curve deviates from linearity. A second peak in velocity was then seen slightly prior to the peak load, with crack-tip velocity reaching approximately 470 μm/s before dropping sharply again as the peak load was reached.

Despite the differences in material and orientation, the crack-tip velocities and failure loads are very similar. Comparison between Figures 4 and 5 demonstrate that the fracture path seen in the Divider orientation Kimmeridge clay sample is much less tortuous than that in the Short-Transverse Mancos shale, where the fractures are prone to following the interfaces between silt and clay layers. The matrix of the Kimmeridge shale material is also substantially richer in clays and organic matter than is the Mancos shale, hence the developing fracture is less likely to be arrested by a localized high-resistance feature. However, the velocities ($\frac{dy}{dt}$) observed in the two samples are very similar, despite the fracture in the Mancos shale deflecting more in the *x* direction.

6. Conclusions

Fracture toughness has been measured in one or two of the three principal crack orientations for six different types of shale, as well as Pennant sandstone. In each shale, the Arrester or Divider orientation displays a higher K_{Ic} value than the Short-Transverse orientation, with $K_{Ic,Div/Arr}/K_{Ic,S-T}$ ratios varying between 1.3 and 6. Pennant sandstone behaved isotropically. The values of K_{Ic} measured here are on a similar order to those previously reported in the literature, and the same trend in K_{Ic} anisotropy was observed.

Stereo optical DIC was used to characterize the strain fields on the surface of the samples and the scale of the inelastic zone size around the fracture-tip in relation to sample size. The inelastic zone size radii (r_Y) were calculated in the Whitby mudstone, Mancos shale, and Pennant sandstone, and r_Y values were found to be in the region of ≃30 μm. This is one to two orders of magnitude smaller than the critical radius assumption of Schmidt (1980), which finds r_c values in the region of ≃ 0.8 mm in the same materials. The r_Y suggests that inelastic deformation is confined to a region around the fracture-tip which is approximately $\frac{1}{100}$ of the sample thickness, while r_c suggests that the inelastic zone radius can be up to one third of the sample thickness. If these smaller zones of inelastic deformation, r_Y are truly the case, then the region of increased permeability around a shale fracture could be an order of magnitude smaller than expected from the model of Schmidt,. This inelastic deformation zone could potentially be investigated further by SEM imaging of the sample surfaces.

Optical DIC also provided a valuable form of quality control when conducting mechanical experiments using this type of complex inhomogeneous material. Mechanical experiments commonly assume no deformation away from a specific region or plane, and the DIC strain fields were able to identify experiments where this was not the case, even in situations where the deformation was not apparent by visual inspection of the sample surface. This type of analysis is potentially very valuable in the continued investigation of the mechanical properties of shale materials, with their strong heterogeneity and anisotropy.

Crack-tip velocity and CMOD were tracked directly using radiograph imaging. The resolvable crack-tip was found to travel at speeds on the order of 100 μm/s during loading, with fractures appearing to travel at approximately the same velocity in the Divider and Short-Transverse orientations, and in Mancos and Kimmeridge shales. Inspection of the samples showed that the Short-Transverse orientation fractures were significantly more tortuous than those in the Divider orientation. This suggests that while a fracture traveling parallel to bedding may travel at a similar speed to a bedding perpendicular fracture, it may take a more tortuous pathway, and therefore access a larger surface area. Further work is required to address the impact of elastic anisotropy on crack-kinking and tortuosity, as the analyses previously applied by Chandler et al. (2016) and Forbes Inskip et al. (2018) simply assume that the effect of elastic anisotropy is small in comparison to that of

the K_{Ic} anisotropy. The variation of the elasticity tensor in shale with depth could potentially be investigated in the laboratory using ultrasonic velocities.

The DIC and radiograph observations combine with the mechanical data presented here to provide new insight into the propagation of fractures in complex inhomogeneous materials. Stereo optical DIC has been shown to allow the determination of yielding regions within shales, while also providing a valuable form of quality control for mechanical deformation experiments. Radiograph imaging has been shown to provide the possibility of tracking the fracture-tip location through complex materials during mechanical experiments.

K_{Ic} anisotropy has now been observed in shales consistently over a number of studies, but further work is required to address how this anisotropy affects the propagation of a fluid-driven subsurface fracture. Modeling suggests that fluid-driven fractures should propagate in the "toughness dominated" regime when fluid pressure has been allowed to equilibrate throughout the fracture, either due to a long timescale or a low-viscosity fluid (Garagash, 2006; Zia et al., 2018). Therefore, the variation in form of fluid injection fractures with injected fluid viscosity might provide some experimental evidence of the influence of K_{Ic} anisotropy in the different regimes.

References

Andrews, I. (2013). *The Carboniferous Bowland Shale gas study: Geology and resource estimation*. London, UK: British Geological Survey for Department of Energy and Climate Change.

Ashby, D., & Pearson, M. (1979). Mineral distributions in sediments associated with the Alton Marine Band near Penistone, South Yorkshire. In D. Ashby, & M. Pearson (Eds.), *International clay conference 1978, developments in sedimentology* (Vol. 27, pp. 311–321). Amsterdam, Netherlands: Elsevier. https://doi.org/10.1016/S0070-4571(08)70727-1

Ayatollahi, M., & Aliha, M. (2008). On the use of Brazilian disc specimen for calculating mixed mode I–II fracture toughness of rock materials. *Engineering Fracture Mechanics*, *75*(16), 4631–4641.

Becker, T., Marrow, T., & Tait, R. (2011). An evaluation of the double torsion technique. *Experimental Mechanics*, *51*(9), 1511–1526.

Burns, C. (2011). Shale gas—A global overview, *Shale gas: Challenging the frontiers of E&P*. London: Society of Petroleum Engineers.

Chandler, M. R., Meredith, P. G., Brantut, N., & Crawford, B. R. (2016). Fracture toughness anisotropy in shale. *Journal of Geophysical Research: Solid Earth*, *121*, 1706–1729. https://doi.org/10.1002/2015JB012756

Chandler, M. R., Meredith, P. G., Brantut, N., & Crawford, B. R. (2017). Effect of temperature on the fracture toughness of anisotropic shale and other rocks. *Geological Society, London, Special Publications*, *454*, 295–303. https://doi.org/10.1144/SP454.6

Chen, X., Eichhubl, P., & Olson, J. E. (2017). Effect of water on critical and subcritical fracture properties of Woodford shale. *Journal of Geophysical Research: Solid Earth*, *122*, 2736–2750. https://doi.org/10.1002/2016JB013708

Chidsey, T., & Morgan, C. (2010). Utah shale gas activity update 2010. In *EMD Annual Leadership Meeting - Gas Shale Committee Report* (pp. 25–27). Tulsa: Energy Minerals Division, AAPG.

Chong, K. P., Kuruppu, M. D., & Kuszmaul, J. S. (1987). Fracture toughness determination of layered materials. *Engineering Fracture Mechanics*, *28*(1), 43–54. https://doi.org/10.1016/0013-7944(87)90118-4

Costin, L. (1981). *Static and dynamic fracture behaviour of oil shale* (pp. 169–184). PA: ASTM Special Technical Publication.

Dowey, P. J., & Taylor, K. G. (2017). Extensive authigenic quartz overgrowths in the gas-bearing Haynesville-Bossier Shale, USA. *Sedimentary Geology*, *356*, 15–25. https://doi.org/10.1016/j.sedgeo.2017.05.001

Eseme, E., Urai, J., Krooss, B., & Littke, R. (2007). Review of mechanical properties of oil shales: Implications for exploitation and basin modelling. In *Oil shale*. TX: Estonian Academic Publishers.

Evans, A. G. (1972). A method for evaluating the time-dependent failure characteristics of brittle materials—and its application to polycrystalline alumina. *Journal of Materials Science*, *7*(10), 1137–1146. https://doi.org/10.1007/BF00550196

Evans, A. G. (1973). A simple method for evaluating slow crack growth in brittle materials. *International Journal of Fracture*, *9*(3), 267–275. https://doi.org/10.1007/BF00049195

Fauchille, A.-L., Hedan, S., Valle, V., Pret, D., Cabrera, J., & Cosenza, P. (2016). Multi-scale study on the deformation and fracture evolution of clay rock sample subjected to desiccation. *Applied Clay Science*, *132*, 251–260.

Fauchille, A., Ma, L., Rutter, E., Chandler, M., Lee, P., & Taylor, K. (2017). An enhanced understanding of the Basinal Bowland shale in Lancashire (UK), through microtextural and mineralogical observations. *Marine and Petroleum Geology*, *86*, 1374–1390. https://doi.org/10.1016/j.marpetgeo.2017.07.030

Fisher, K., & Warpinski, N. (2012). Hydraulic-fracture-height growth: Real data. *SPE Production & Operations*, *27*(1), 8–19.

Forbes Inskip, N. D., Meredith, P. G., Chandler, M. R., & Gudmundsson, A. (2018). Fracture properties of Nash Point shale as a function of orientation to bedding. *Journal of Geophysical Research: Solid Earth*, *123*, 8428–8444. https://doi.org/10.1029/2018JB015943

Fuller, E. (1979). An evaluation of double-torsion testing—Analysis. In S. Freiman (Ed.), *Fracture mechanics applied to brittle materials* pp. 3–18). Philadelphia: American Society for Testing and Materials.

Garagash, D. I. (2006). Plane-strain propagation of a fluid-driven fracture during injection and shut-in: Asymptotics of large toughness. *Engineering Fracture Mechanics*, *73*(4), 456–481. https://doi.org/10.1016/j.engfracmech.2005.07.012

Giger, S., & Marschall, P. (2014). *Geomechanical properties, rock models and in-situ stress conditions for Opalinus Clay in Northern Switzerland*. Switzerland: Arbeitsbericht NAB 14-01, Nagra Wettingen.

Hackston, A., & Rutter, E. (2016). The Mohr–coulomb criterion for intact rock strength and friction—A re-evaluation and consideration of failure under polyaxial stresses. *Solid Earth*, *7*(2), 493–508. https://doi.org/10.5194/se-7-493-2016

Hammes, U., & Frébourg, G. (2012). Haynesville and Bossier mudrocks: A facies and sequence stratigraphic investigation, East Texas and Louisiana, USA. *Marine and Petroleum Geology*, *31*(1), 8–26.

Hawthorn, D. (2004). An experimental study of the permeability of Kimmeridge Clay Mudstone (Ph.D. thesis), University of Manchester.

Janssen, M., Zuidema, J., & Wanhill, R. (2002). *Fracture mechanics* (2nd ed.). The Netherlands: VSSD, Delft.

Kabir, P., Ulm, F.-J., & Akono, A.-T. (2017). Rate-independent fracture toughness of gray and black kerogen-rich shales. *Acta Geotechnica*, *12*, 1207–1227. https://doi.org/10.1007/s11440-017-0562-0

Keller, L. M., Schwiedrzik, J. J., Gasser, P., & Michler, J. (2017). Understanding anisotropic mechanical properties of shales at different length scales: In situ micropillar compression combined with finite element calculations. *Journal of Geophysical Research: Solid Earth*, *122*, 5945–5955. https://doi.org/10.1002/2017JB014240

Kelling, G. (1974). *Upper carboniferous sedimentation in south Wales*.

Khazan, Y. M., & Fialko, Y. A. (1995). Fracture criteria at the tip of fluid-driven cracks in the Earth. *Geophysical Research Letters*, *22*(18), 2541–2544. https://doi.org/10.1029/95GL02547

Lee, H. P., Olson, J. E., Holder, J., Gale, J. F. W., & Myers, R. D. (2015). The interaction of propagating opening mode fractures with preexisting discontinuities in shale. *Journal of Geophysical Research: Solid Earth*, *120*, 169–181. https://doi.org/10.1002/2014JB011358

Longman, M., & Koepsell, R. (2005). Defining and characterizing Mesaverde and Mancos sandstone reservoirs based on interpretation of Formation Microimager (FMI) logs.

Luo, Y., Xie, H., Ren, L., Zhang, R., Li, C., & Gao, C. (2018). Linear elastic fracture mechanics characterization of an anisotropic shale. *Scientific Reports*, *8*(1), 8505.

Ma, L., Slater, T., Dowey, P. J., Yue, S., Rutter, E. H., Taylor, K. G., & Lee, P. D. (2018). Hierarchical integration of porosity in shales. *Scientific Reports*, *8*(1), 11683.

Masoudian, M. S., Hashemi, M. A., Tasalloti, A., & Marshall, A. M. (2018). Elastic–brittle–plastic behaviour of shale reservoirs and its implications on fracture permeability variation: An analytical approach. *Rock Mechanics and Rock Engineering*, *51*(5), 1565–1582. https://doi.org/10.1007/s00603-017-1392-y

McClintock, F. A., & Irwin, G. (1965). Plasticity aspects of fracture mechanics, *Fracture toughness testing and its applications*. Pennsylvania, United States: ASTM International.

McKernan, R., Mecklenburgh, J., Rutter, E., & Taylor, K. (2017). Microstructural controls on the pressure-dependent permeability of Whitby mudstone. *Geological Society, London, Special Publications*, *454*, 39–66. https://doi.org/10.1144/SP454.15

McKernan, R., Rutter, E., Mecklenburgh, J., Taylor, K., & Covey-Crump, S. (2014). Influence of effective pressure on mudstone matrix permeability: Implications for shale gas production. In *SPE/EAGE European Unconventional Resources Conference and Exhibition*, Society of Petroleum Engineers, pp. 25–27.

Pan, B., Qian, K., Xie, H., & Asundi, A. (2009). Two-dimensional digital image correlation for in-plane displacement and strain measurement: A review. *Measurement Science and Technology*, *20*(6), 062001.

Rawson, P. F., & Wright, J. K. (1995). Jurassic of the Cleveland Basin, North Yorkshire. In P. Taylor (Ed.), *Field geology of the British Jurassic* pp. 173–208). London: Geological Society.

Reu, P. (2012a). Stereo-rig design: Creating the stereo-rig layout — Part 1. *Experimental Techniques*, *36*(5), 3–4. https://doi.org/10.1111/j.1747-1567.2012.00871.x

Reu, P. (2012b). Hidden components of DIC: Calibration and shape function — Part 1. *Experimental Techniques*, *36*(2), 3–5.

Reu, P. (2012c). Hidden components of 3D-DIC: Triangulation and post-processing — Part 3. *Experimental Techniques*, *36*(4), 3–5.

Rice, J. (1974). Limitations to the small scale yielding approximation for crack tip plasticity. *Journal of the Mechanics and Physics of Solids*, *22*(1), 17–26. https://doi.org/10.1016/0022-5096(74)90010-6

Rutter, E., Mecklenburgh, J., & Taylor, K. (2017). Geomechanical and petrophysical properties of mudrocks: Introduction. *Geological Society, London, Special Publications*, *454*, 1–13. https://doi.org/10.1144/SP454.16

Schindelin, J., Arganda-Carreras, I., Frise, E., Kaynig, V., Longair, M., Pietzsch, T., et al. (2012). Fiji: An open-source platform for biological-image analysis. *Nature methods*, *9*(7), 676–82.

Schmidt, R. A. (1980). A microcrack model and its significance to hydraulic fracturing and fracture toughness testing. In *The 21st US Symposium on Rock Mechanics (USRMS)* (pp. 581–590). American Rock Mechanics Association.

Schmidt, R., & Huddle, C. (1977). Fracture mechanics of oil shale: Some preliminary results (pp. 1–29). *Sandia Laboratories*.

Shyam, A., & Lara-Curzio, E. (2006). The double-torsion testing technique for determination of fracture toughness and slow crack growth behavior of materials: A review. *Journal of Materials Science*, *41*(13), 4093–4104. https://doi.org/10.1007/s10853-005-5553-0

Sutton, M. A., Orteu, J. J., & Schreier, H. (2009). *Image correlation for shape, motion and deformation measurements: Basic concepts, theory and applications*. New York: Springer Science & Business Media.

Swanson, P. L. (1984). Subcritical crack growth and other time- and environment-dependent behavior in crustal rocks. *Journal of Geophysical Research*, *89*(B6), 4137–4152. https://doi.org/10.1029/JB089iB06p04137

Tait, R. B., Fry, P. R., & Garrett, G. G. (1987). Review and evaluation of the double-torsion technique for fracture toughness and fatigue testing of brittle materials. *Experimental Mechanics*, *27*(1), 14–22. https://doi.org/10.1007/BF02318858

Thiercelin, M., Jeffrey, R., & Naceur, K. B. (1989). Influence of fracture toughness on the geometry of hydraulic fractures. In *SPE Production Engineering*, pp. 435–442.

Wang, C., & Pilliar, R. (1989). Short-rod elastic-plastic fracture toughness test using miniature specimens. *Journal of Materials Science*, *24*(7), 2391–2400. https://doi.org/10.1007/BF01174501

Warpinski, N., & Smith, M. (1990). Rock mechanics and fracture geometry. In J. Gidley, S. Holditch, D. Nierode, & R. Veatch (Eds.), *Recent advances in hydraulic fracturing* pp. 57–80). Texas: Society of Petroleum Engineers.

Williams, D., & Evans, A. (1973). A simple method for studying slow crack growth. *Journal of testing and evaluation*, *1*(4), 264–270.

Yang, Z., Wang, L., Zhang, G., & Ho, C. (2016). Micromechanical characterization of fluid-shale interactions via nanoindentation. In *SPE Asia Pacific Hydraulic Fracturing Conference*, Society of Petroleum Engineers, pp. 24–26.

Young, C., Patti, N., & Trent, B. (1982). Stratigraphic variations in oil shale fracture properties. *US DOE Report of Investigation*, 1–22.

Zia, H., Lecampion, B., & Zhang, W. (2018). Impact of the anisotropy of fracture toughness on the propagation of planar 3D hydraulic fracture. *International Journal of Fracture*, *211*(1), 103–123. https://doi.org/10.1007/s10704-018-0278-7